

Concentration effect of TEMPO-oxidized nanofibrillated cellulose aqueous suspensions on the flow instabilities and small-angle X-ray scattering structural characterization

Oleksandr Nechyporchuk · Mohamed Naceur Belgacem ·
Frédéric Pignon

Received: 12 January 2015 / Accepted: 25 April 2015 / Published online: 5 May 2015
© Springer Science+Business Media Dordrecht 2015

Abstract The rheological behavior of 2,2,6,6-tetramethylpiperidine-1-oxyl (TEMPO)-oxidized nanofibrillated cellulose (NFC) suspensions at different concentrations were examined using Couette with smooth and serrated surfaces and vane-in-cup geometries. A slippage against the walls of rheometer rotor or/and stator (wall-slip) as well as flow localization within a specific volume of the sample (shear banding) took place. These phenomena were visualized using a technique based on introduction of titanium dioxide pigment into the specific volume of NFC suspension and monitoring its deformation. The flow instabilities appeared more pronounced with an increase of the NFC concentration. It was shown that the use of serrated geometry is necessary to compete

with the wall-slip but is not sufficient to prevent it completely. Serrated Couette was found to be the most appropriate geometry (among the tested) to measure the rheological properties of NFC suspensions. Small-angle X-ray scattering was used to provide a supplementary information about the structural organization of NFC suspensions. The statistical average diameter of 4.8 nm was determined from the scattering data for the NFC swollen in water.

Keywords Nanofibrillated cellulose (NFC) · Microfibrillated cellulose (MFC) · TEMPO-oxidized cellulose nanofibers (TOCN) · Rheology · Wall-slip · Shear banding

O. Nechyporchuk · F. Pignon
Université Grenoble Alpes, LRP, F-38000 Grenoble,
France
e-mail: oleksandr.nechyporchuk@lgp2.grenoble-inp.fr

O. Nechyporchuk · F. Pignon (✉)
CNRS, LRP, F-38000 Grenoble, France
e-mail: frederic.pignon@ujf-grenoble.fr

O. Nechyporchuk · M. N. Belgacem
Université Grenoble Alpes, LGP2, F-38000 Grenoble,
France

O. Nechyporchuk · M. N. Belgacem
CNRS, LGP2, F-38000 Grenoble, France

O. Nechyporchuk · M. N. Belgacem
Agefpi, LGP2, F-38000 Grenoble, France

Introduction

The last years have become a real breakthrough in commercial production of nanofibrillated cellulose (NFC) and this progress seems only to expand. Today NFC is already available in the market as a commercial product and gains much interest for industrial application in such areas as papermaking, paints and coatings, composites, pharmaceuticals and cosmetics, food etc.

NFC is commonly produced in the form of aqueous suspensions. Therefore, their rheological properties become a key issue, since the flow is involved in the production process and can influence the performance of the NFC-containing products. Consequently, the

control of the flow behavior of NFC suspensions becomes highly desirable. Moreover, the rheological properties give an insight into the structure of a material. For instance, Ishii et al. (2011) reported a method for determination of the average length of 2,2,6,6-tetramethylpiperidine-1-oxyl (TEMPO)-oxidized NFC based on the rheological measurements. A more comprehensive analysis of structural properties of NFC suspensions can be performed using scattering techniques, e.g., small-angle X-ray scattering (SAXS).

NFC, otherwise known as microfibrillated cellulose (MFC) or cellulose nanofibers (CNF), was first produced in the early 1980s by mechanical disintegration of cellulose fibers using a high-pressure homogenizer (Turbak et al. 1983). The rheological properties of such NFC suspensions were reported at the same time (Herrick et al. 1983), describing the gel-like and shear thinning behavior at 2 wt% cellulose concentration. Since then, various methods have been investigated to facilitate the nanofibrils separation during mechanical processing and to reduce the energy demand required for their isolation. The modern methods involve mainly enzymatic or chemical pretreatments followed by the mechanical disintegration. The conversion of the primary hydroxyl groups of cellulose monomer to carboxyl moieties through TEMPO-mediated oxidation (Saito et al. 2006) is one of the commonly used chemical pretreatments. Such oxidation process facilitates significantly the nanofibrils isolation due to electrostatic repulsion between the carboxylate ions formed on the surface of cellulose nanofibrils (at neutral and/or basic conditions).

The rheological properties of the different types of NFC suspensions have been studied, e.g., enzymatically hydrolyzed (Pääkkö et al. 2007; Charani et al. 2013), TEMPO-oxidized (Saito et al. 2007; Lasseguette et al. 2008; Benhamou et al. 2014), carboxymethyl (Naderi et al. 2014). It has been reported that the viscosity increases sharply with a slight increase of cellulose concentration (Pääkkö et al. 2007; Agoda-Tandjawa et al. 2010; Shogren et al. 2011). The higher viscosities are acquired with more intense fibrillation (Lasseguette et al. 2008).

Rheological studies of different NFC-based products have been published. For instance, the properties of NFC suspensions from sugar beet pulp mixed with polyelectrolytes, as a potential thickening systems for food applications, were studied by Lowys et al. (2001).

A melt rheology of nanofibrillated cellulose/acrylic polymer nanocomposites was examined by Besbes et al. (2011). Grüneberger et al. (2014) performed the rheological characterization of NFC/acrylate systems for wood coatings.

The continuous research in this field revealed the problems of flow fluctuations, which cause a distortion of the rheological measurements. NFC suspensions tend to slip against smooth walls of the rheometer rotor or stator. Moreover, during flow measurements the deformation can be localized within a specific volume of the sample, called shear banding. The problems of the wall-slip and shear banding in NFC suspensions were mentioned in several works (Saarinen et al. 2009; Saarikoski et al. 2012; Puisto et al. 2012; Mohtaschemi et al. 2014). In order to compete with the wall-slip in NFC suspensions Iotti et al. (2011) used parallel plate geometry with a roughened base plate; Charani et al. (2013) applied roughened rotor and stator plates; Naderi et al. (2014) used serrated bob and cup; Mohtaschemi et al. (2014) described a use of wide-gap vane geometry. These were believed to minimize the slip on the contact surface between geometry tools and NFC suspension. However, to the best of our knowledge, no work was reported to study whether these instruments were efficient to prevent the flow instabilities in NFC suspensions.

Recently, we have reported the production (Nechyporchuk et al. 2015) and rheological characterization (Nechyporchuk et al. 2014) of different grade NFC suspensions, prepared using enzymatic and TEMPO-oxidation pretreatments. During the rheological measurements the wall-slip and shear banding phenomena were first demonstrated using a visualization technique, where a thin vertical filament of NFC, colored with titanium dioxide (TiO₂), was introduced inside the investigated NFC for monitoring the sample deformation when using cone-plate geometry. Roughening of the geometry surfaces was performed to overcome the wall-slip and was efficient for the TEMPO-oxidized NFC. The experiments were performed for this sample at the concentration of 1 wt%; however, the study of the occurrence of the flow instabilities at other concentrations is of great interest.

In this work the above concept of strain field monitoring using TiO₂ pigment was implemented in concentric cylinder (Couette) with smooth and serrated surfaces and vane-in-cup geometries with the aim of studying the flow instabilities occurring in TEMPO-

oxidized NFC at different concentrations. Since TiO_2 possesses a very high refractive index (~ 2.7), it was used to impart white opacity to a certain volume of the sample and to monitor its deformation. The advantage of Couette geometry is the possibility of studying the dilute suspensions, as well as testing the suspensions with the large particles. Vane-in-cup geometry induces a minimal disturbance of the sample when inserting the tool. Moreover, the recent studies claimed (Mohtaschemi et al. 2014) that the wall-slip can be avoided when using wide-gap vane-in-cup geometry for testing of NFC suspensions.

The complex entangled structure of nanofibrillated cellulose suspensions is the main reason of the flow instabilities emergence, induced during the rheological measurements. The structural properties of NFC suspensions are determined particularly by cellulose nanofibrils morphology, which is commonly studied using microscopy techniques, e.g., atomic force microscopy (AFM), transmission electron microscopy (TEM). However, these techniques are based on a selective analysis of some portion of the sample. Moreover, the cellulose samples are typically used in a dry state for such analysis. To evaluate the size, shape and orientation of particles in suspension, SAXS can be used. This technique is based on a statistical average over a large amount of scattering objects in suspension.

The SAXS studies were reported for the suspensions of cellulose nanocrystals (Terech et al. 1999; Bonini et al. 2002; Elazzouzi-Hafraoui et al. 2008) as well as NFC (Leppänen et al. 2010; Penttilä et al. 2013). Leppänen et al. (2010) analyzed the NFC suspension at 10 wt% concentration as well as in dry and re-wet states. Penttilä et al. (2013) have focused their studies on structural changes of NFC during enzymatic hydrolysis.

Here we perform SAXS measurements on dilute NFC aqueous suspensions of 0.1 and 0.5 wt%, for minimizing the interparticle interferences, in order to determine the dimensions of cellulose nanofibrils and examine their structural organization.

Materials and methods

NFC production

TEMPO-oxidized NFC suspensions were produced as reported earlier (Nechyporchuk et al. 2015).

Briefly, bleached softwood bisulfite pulp (Quality 2100, Domsjö Fabriker AB) was soaked in deionized water during 4 h and dispersed using a standard disintegrator according to ISO 5263-1:2004. TEMPO-mediated oxidation was performed according to the method reported by Saito et al. (2007). Cellulose was oxidized at the concentration of 1 wt% in water, containing TEMPO/NaBr/NaClO (0.1/1/5 mmol per gram of cellulose, respectively), at the temperature of 25 °C and pH of 10 ± 0.1 . The pH was maintained stable by the addition of NaOH till no longer decrease of the pH was observed, indicating that no longer formation of carboxyl groups takes place. The reaction was quenched by lowering the pH till 7 using HCl.

The oxidized cellulose was washed on a Büchner funnel using a nylon sieve with the mesh size of 1 μm and redispersed in water at the concentration of 1.5 wt%. The obtained cellulose suspension was fibrillated through ultra-fine friction grinder Supermasscolloider (model MKZA6-2, grinding stones MKG-C80, Masuko Sangyo Co., Ltd., Japan) at 2500 rpm for 60 passes. The produced NFC gel was used at concentrations of 0.5, 1.0 and 1.5 wt%. The dilution was performed using deionized water. The samples were stored at the temperature of 4 °C.

Rheological measurements

The rheological measurements were performed using a stress-controlled rheometer DHR-3 (TA Instruments) equipped with (a) Couette (recessed concentric cylinders with smooth surfaces; roughness of $\sim 0.8 \mu\text{m}$; cup diameter of 37 mm; bob diameter of 28 mm; operating gap of 4 mm); (b) serrated Couette (manufactured by gluing sandpaper using twofold adhesive tape to the bob and cup surfaces of the above Couette; roughness of $\sim 120 \mu\text{m}$, resulting cup diameter of 36.2 mm; bob diameter of 28.8 mm); or (c) vane-in-cup (cup diameter of 37 mm; four-blade vane: diameter of 10 mm, height of 19 mm; operating gap of 37 mm) geometries.

Before starting the experiments, the samples were kept overnight at room temperature. After the insertion into the rheometer they were allowed to rest for 5 min to minimize the shear history arising from the sample loading. The samples were not presheared in the rheometer, which is commonly done to eliminate the thixotropy effect, since the high shearing forces fracture the sample, creating bands of stagnating and

flowing suspensions, especially for highly concentrated suspensions. Moreover, at low shear rates wall-slip appears. Thus, the initial NFC structure can be distorted before the measurements. Moreover, some time was necessary to introduce TiO_2 pigment inside the sample, making it not possible to analyze the sample just after preshear. Each measurement was performed thrice and an average value was calculated.

Oscillation flow experiments of the suspensions at different concentrations were performed using smooth Couette geometry. The strain sweeps were conducted in the range of 0.01–10 % at a frequency of 1 Hz to define the strain corresponding to the linear domains of the deformation. Then, the frequency sweeps in the range of 0.1–100 rad/s at strain of 0.1 %, defined from the linear domains, were performed.

Steady flow measurements were carried out using smooth and serrated Couette and vane-in-cup geometries with an introduced filament of the suspension colored with TiO_2 , as shown in Fig. 1. The deformation of this filament was monitored using CCD camera. For the interpretation of the shear flow in the vane-in-cup geometry, it was assumed that: (a) the stress distribution is uniform over the cylindrical sheared surface, described by the outer edges of the blades; (b) the NFC suspension trapped between the blades of vane geometry behaves as a rigid material

and there is no secondary flow between the blades. Therefore, the sample was analyzed similarly to that tested using Couette geometry. Despite the different methods were reported to improve the accuracy of the shear flow measurements from vane-in-cup geometry (Baravian et al. 2002; Estellé et al. 2008), here the main purpose was to investigate the possible flow instabilities using visualization approach.

SAXS measurements

The SAXS experiments were performed on ID2 high brilliance beamline at European Synchrotron Radiation Facility (ESRF, Grenoble, France). Dilute TEMPO-oxidized NFC suspensions (0.1 and 0.5 wt%) were analyzed under controlled temperature (25 ± 1 °C). The samples were introduced in a flow-through capillary cell (diameter ~ 2 mm) and were further measured at rest. An incident monochromatized X-ray beam at wavelength of 0.995 Å was used. Scattered intensities were recorded on a two-dimensional CCD detector at sample-to-detector distances of 1 and 10 m. The scattering intensity distribution as a function of scattering vector was obtained by radial integration of two-dimensional (2D) scattering pattern. The scattering data of cell filled with water was subtracted as a background from the intensity of the suspension yielding the

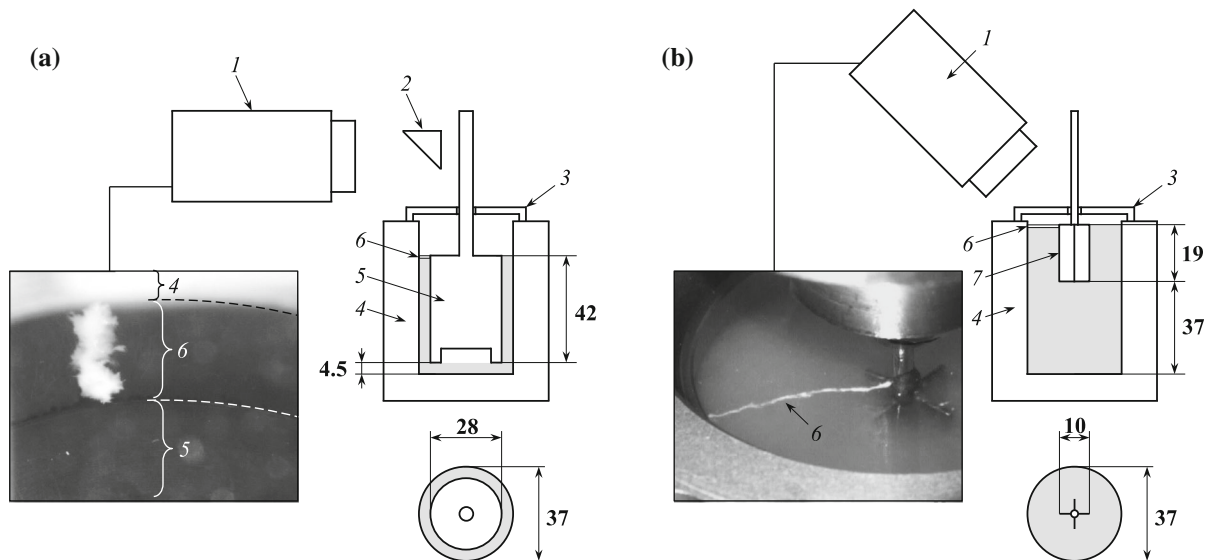


Fig. 1 Schematic diagrams of Couette (a) and vane-in-cup (b) setups for the rheological measurements combined with the visualization of the sample deformation: (1) CCD camera; (2) mirror; (3) transparent cup to prevent water evaporation; (4)

cup; (5) bob; (6) filament of NFC suspension colored with titanium dioxide pigment; (7) vane. The dimensions (mm) are shown in *bold*

information about the NFC. The scattering curves at different sample-to-detector distances were superimposed. The unified fit function was modeled using Irena software (Ilavsky and Jemian 2009).

Analysis of SAXS data

During SAXS experiment the sample was irradiated by X-rays and the intensity of scattered beam at low angular range was analyzed. The magnitude of the scattering vector (q), is related to the scattering angle, as follows (Eq. 1):

$$q = \left(\frac{4\pi}{\lambda}\right) \sin \theta, \quad (1)$$

where λ is the wavelength of X-rays and θ is a half of the scattering angle.

When plotting the scattered intensity (I) as a function of scattering vector at logarithmic scales, a power-law dependence (Eq. 2) yields the fractal dimensions (D) of the scattering objects at the particular length scale, yielding the information about the particle shape.

$$I(q) \propto q^{-D}. \quad (2)$$

If there is no interparticle interference (e.g., in very dilute suspensions), Guinier approximation (Glatter and Kratky 1982) can be applied for the size determination of the scattering objects (Eq. 3):

$$I(q) = I_0 \exp\left(\frac{-R_g^2 q^2}{3}\right), \quad (3)$$

where R_g is a radius of gyration, which represents an effective size of the scattering object. R_g can be determined by plotting $\ln[I(q)]$ versus q^2 , the so-called Guinier plot. When yielding a linear behavior, the slope is equal to $-R_g^2/3$. The Guinier approximation is valid for $qR_g \leq 1$, indicating that the objects are smaller than the probed range. Thus, the objects constituting one structural level, e.g., non-aggregated spherical particles, can be described by Guinier and a power-law regime.

Individualized elongated particles exhibit two structural levels: there is scattering coming from the whole particle, and the one associated with the particle cross-section. Thus, two Guinier laws and two power laws describe the structure of the scattering objects. In

this case Guinier laws appear as: (a) Guinier approximation at lower q , representing the scattering coming from the particle, as described by (Eq. 3) and (b) Guinier approximation at higher q , relative to the particle cross-section, described as follows (Eq. 4):

$$I(q) = \frac{I_0}{q} \exp\left(\frac{-R_{gc}^2 q^2}{2}\right), \quad (4)$$

where R_{gc} is a radius of gyration of the particle cross-section. R_{gc} can be determined by plotting $\ln[q I(q)]$ versus q^2 , where the slope of the curve is equal to $-R_{gc}^2/2$. Here, when multiplying the $I(q)$ by q , the factor of the particle length is eliminated and the obtained curve represents the information associated with the cross-section only (Glatter and Kratky 1982). From the R_{gc} the particle radius (r) can be calculated according to Eq. (5):

$$R_{gc}^2 = \frac{r^2}{2}. \quad (5)$$

For the rod-like particles the length (l) can be calculated from the R_g using Eq. (6):

$$R_g^2 = \frac{l^2}{12} + \frac{r^2}{2}. \quad (6)$$

For complex hierarchical systems, consisting of overlapped structural levels, e.g., polydisperse aggregated particles, a unified fit function (Beaucage function) can be used (Beaucage 1995, 1996) to analyze the small-angle scattering data. The unified function (Eq. 7) consists of the scattering functions from n structural levels, each containing a Guinier regime representing the $R_{g,i}$, and a power-law regime reflecting the type of the analyzed structure:

$$I(q) = \sum_{i=1}^n \left(G_i \exp\left(-\frac{q^2 R_{g,i}^2}{3}\right) + B_i \exp\left(-\frac{q^2 R_{g,i-1}^2}{3}\right) \times \left(\frac{[\operatorname{erf}(kqR_{g,i}/\sqrt{6})]^3}{q}\right)^{P_i} \right), \quad (7)$$

where G is a Guinier prefactor; B is a power-law prefactor; $\operatorname{erf}()$ is an error function; $k = 1$ for $P > 3$ or $k = 1.06$ for $1.5 \lesssim P \lesssim 3$ and P is an exponent reflecting the power-law scattering (Beaucage 1996). The function describes a system, where $i = 1$ is a primary structural level composed of the smallest scattering objects at high q ; and $i = n$ at low

q represents the largest scattering objects, which can be composed from the elements from the previous structural levels.

For the rod-like particles the radius (r) and length (l) can be calculated from the radii of gyration at the first and second structural levels (Beaucage 2012):

$$R_{g,1}^2 = \frac{3}{4}r^2; \quad (8)$$

$$R_{g,2}^2 = \frac{l^2}{12} + \frac{r^2}{2}. \quad (9)$$

Results and discussion

Oscillation measurements

Figure 2 shows the storage and loss moduli (G' and G'' , respectively) as a function of oscillation strain (γ) and oscillation frequency (ω) for the TEMPO-oxidized NFC samples at different concentrations. The storage and loss (dynamic) moduli were plotted while the raw phase was below 90° indicating that no influence of the inertial effects takes place. Figure 2a shows the linear region of the deformation where the G' and G'' are independent of strain up to a critical level ($\sim 1\%$ of strain), beyond which the disruption of the suspension structure occurs, displaying the out of the linear region of the sample deformation. It is obvious that the critical strain level is almost independent of the NFC concentrations.

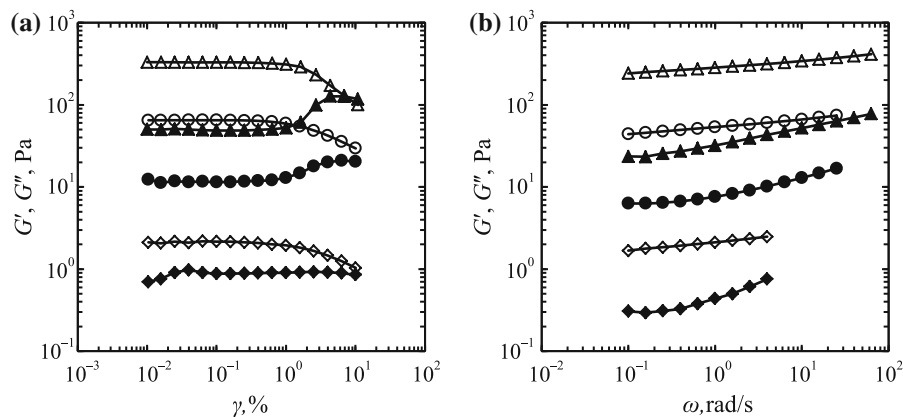


Fig. 2 Storage (*empty symbols*) and loss moduli (*filled symbols*) as a function of: **a** oscillation strain and **b** oscillation frequency for TEMPO-oxidized NFC suspensions at the

Figure 2b shows the dynamic moduli as a function of oscillation frequency measured at a strain (0.1 %) below the critical level. All the suspensions exhibit gel-like properties ($G' \gg G''$). The dynamic moduli increase when increasing the NFC concentration, since the stronger fibrous network is formed, which is in agreement with the other studies (Pääkkö et al. 2007; Agoda-Tandjawa et al. 2010). G' and G'' obtained using Couette geometry are slightly lower comparing to that of cone-plate geometry, as reported previously (Nechyporchuk et al. 2014). This is in agreement with Saarinen et al. (2009), who have studied the influence of the geometry types and geometry gap on the storage modulus. They attributed such differences to the presence of the flocculated structures in the suspension, which have a larger phase volume comparing to that of the individual nanofibrils, hence influencing in a more pronounced manner the measurements at lower gap.

Flow measurements

Couette geometry with smooth surfaces was used in combination with the visual monitoring of the strain field inside the sample, as illustrated above in Fig. 1a, to study the occurrence of flow instabilities in TEMPO-oxidized NFC suspensions, when submitted to a steady shear. Figure 3 shows the corresponding shear stress (σ) versus shear rate ($\dot{\gamma}$) curves for the suspensions at the concentrations of 0.5, 1.0 and 1.5 wt%. Each column of photographs represents the

concentrations of (*empty diamonds, filled diamonds*) 0.5 wt%; (*empty circles, filled circles*) 1.0 wt% and (*empty triangles, filled triangles*) 1.5 wt%, measured using Couette geometry

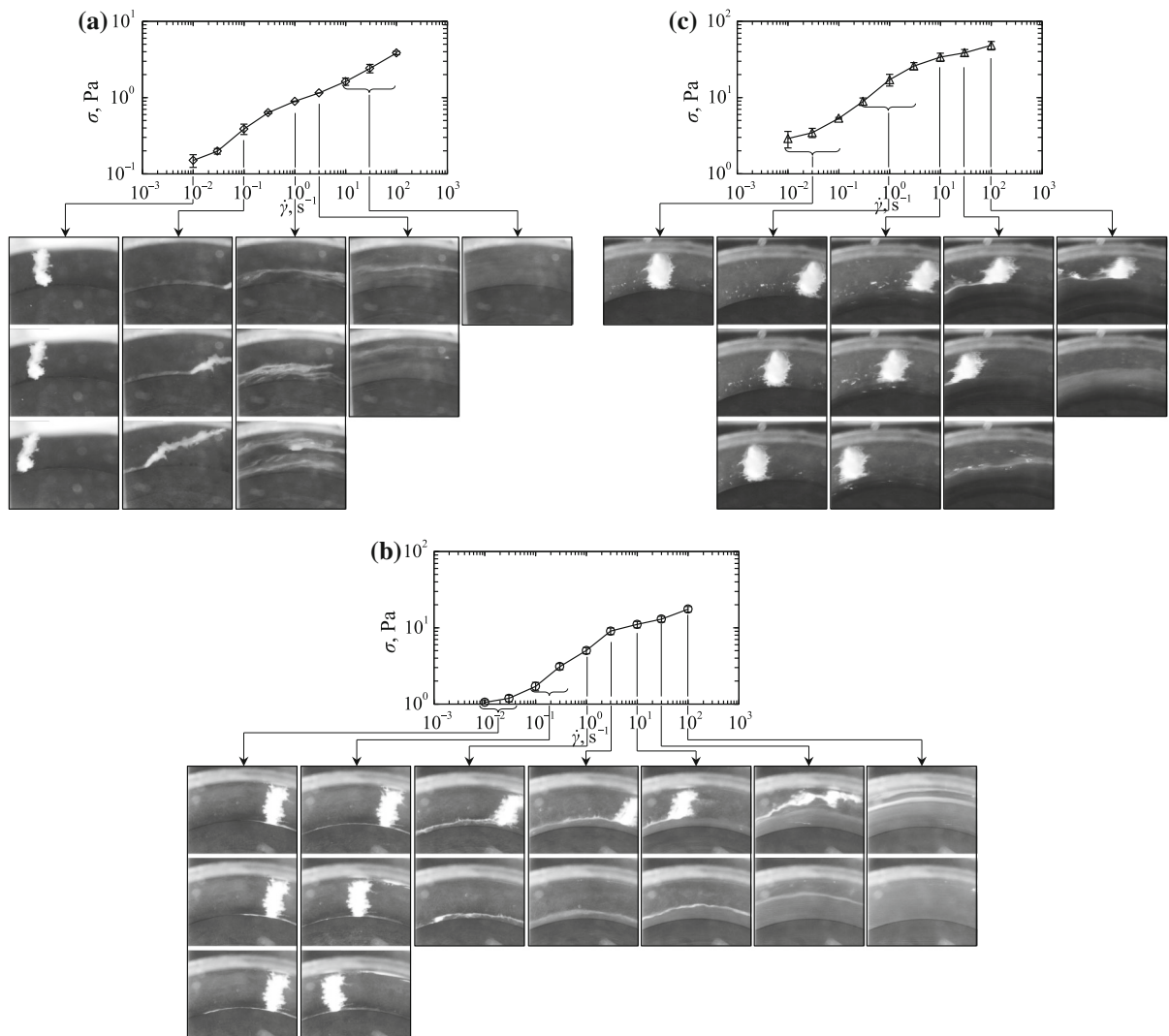


Fig. 3 Flow curves together with strain visualization of TEMPO-oxidized NFC suspensions at the concentrations of: **a** 0.5 wt%, **b** 1.0 wt% and **c** 1.5 wt% examined using Couette geometry. Each column of photographs represents the

characteristic behavior of the sample at a constant shear rate while the strain increases. The photographs of the samples were taken as a function of strain/time. The lower photograph position indicates the higher strain applied. The typical nonlinear rheology of the NFC suspensions is observed. The shear stress increases within all the range of shear rates applied for three tested concentrations.

Figure 3a shows that at the concentration of 0.5 wt% the deformation of the colored filament takes part within all the range of the shear rates. However, at

characteristic behavior of the sample at a constant shear rate while the strain increases. The lower photograph position indicates the higher strain applied

$\dot{\gamma} = 0.1 \text{ s}^{-1}$ it is evident that, despite the deformation took place, a depletion of NFC suspension adjacent to the shearing surfaces of the bob happens, resulting in a wall-slip (white margin at the bob-suspension contact seen in Fig. 3a). Thus, the local strain of the sample is lower than that applied by the rheometer. With an increase of the shear rate, the suspension undergoes a shear banding transition. At $\dot{\gamma} = 1$ and 3 s^{-1} , the sample flows non-homogeneously with a separation of the suspension into regions with different shear rates. The shear banding is characterized by a homogeneous

flow near the bob and a non-homogeneous flow near the cup boundary. At higher shear rates ($10\text{--}100\text{ s}^{-1}$) the flow appears homogeneous within all the gap of the Couette geometry.

The flow instabilities became more pronounced for the NFC suspension at a concentration of 1.0 wt%, as shown in Fig. 3b. At $\dot{\gamma} = 0.01$ and 0.03 s^{-1} a slip at the boundary of the bob and suspension is significant, which impedes the suspension flowing. At $\dot{\gamma} = 0.1$ and 0.3 s^{-1} there is still no deformation of the color filament, but two slips occur at the contact of NFC suspension with bob and cup. The subsequent increase of the shear rate produces a shear banding effect. The magnitude of the flowing volume of the suspension increases with the increase of shear rate. The total deformation of the sample results from a combination of flow and stagnation of some volume of the sample, which slips over the cup surface.

Figure 3c presents the flow experiments of the NFC suspension at 1.5 wt%. At low shear rates ($\dot{\gamma} = 0.01\text{--}0.1\text{ s}^{-1}$) a slip at the boundary of the bob and the suspension appears. At higher shearing forces ($\dot{\gamma} = 0.3\text{--}3\text{ s}^{-1}$) a slip against smooth walls of both bob and cup takes place preserving the NFC sample flow. The higher shear rates produced the bands, consisted of the flowing and stagnating portions of the suspension.

Obviously, such flow instabilities have a significant impact with regard to the measured rheological properties. To avoid these instabilities, different methods can be used. In our previous work (Nechyporchuk et al. 2014) the roughening of the cone and plate surfaces was performed to prevent the wall-slip. The other way to avoid a wall-slip is to use a wide-gap vane-in-cup geometry, as proposed by Mohtaschemi et al. (2014). When using vane geometry, the NFC suspension is sheared by the suspension, trapped between the blades, which is believed to avoid the slip at the edge of vane blades and the sample. The wide gap between the vane and cup is necessary to avoid the wall-slip at the cup surface due to the low stress arising at the cup edge.

Figure 4 shows the shear stress versus shear rate curves combined with the photographs of the sample deformation for the wide-gap vane-in-cup experiments. The use of such geometry was efficient to avoid a slip at vane-sample contact for suspension at a concentration of 0.5 wt%. However, at low shear rates the flow appears only in a thin volume of the sample

close to the vane blades. Only at the shear rate of 100 s^{-1} the deformation within all the gap of the geometry was achieved, as seen from Fig. 4a. Therefore, the measurements are representative of the volume property of the sample only after reaching this shear rate.

Similarly to that of Couette geometry, the flow instabilities became more apparent as the NFC concentration increased. Figure 4b shows that at the concentration of 1.0 wt% the stagnating volume of the sample increases for the equivalent strain applied. At low shear rates ($\dot{\gamma} = 0.01\text{--}0.1\text{ s}^{-1}$) an effect resembling a slip occurs. It appears despite the cohesive forces between the NFC suspension, trapped between the blades, and that of in the geometry gap (between the edge of the blades and the walls of the cup). The sample fractures at the edge of the vane blades and is not subjected to flowing in the gap of the geometry. With an increase of shear rate the shear banding transition occurs producing the stationary and flowing portions of the sample.

Figure 4c shows the flow curves and the deformation visualization of the NFC suspension at the concentration of 1.5 wt%. The similar flow instabilities occur as for the suspension at the concentration of 1.0 wt%; however, the slip is observed for higher range of shear rates. At the shear rates of 10 and 100 s^{-1} only slight volume of the sample is subjected to flow.

It is important to emphasize that these flow instabilities, observed for Couette and vane-in-cup geometries, introduce a strong error in the rheological measurements. The use of wide-gap vane-in-cup geometry prevented the slip effect only for suspension at the concentration of 0.5 wt% and was not efficient for 1.0 and 1.5 wt%. Moreover, strong flow localization occurs affecting the rheological measurements at all the concentrations. Consequently, these measurements should be corrected regarding the true strain of the sample. At the same time such behavior illustrates the ability of the examined TEMPO-oxidized NFC to slip over the smooth shearing surfaces and to fracture at the specific regions where the strain is accumulated.

The obtained results using vane-in-cup geometries are in contradiction with those reported by Mohtaschemi et al. (2014) who tested the TEMPO-oxidized NFC suspensions at the concentrations of 1.0–2.3 wt%, avoiding the wall-slip. However, the comparisons and speculations in this context appear difficult since the

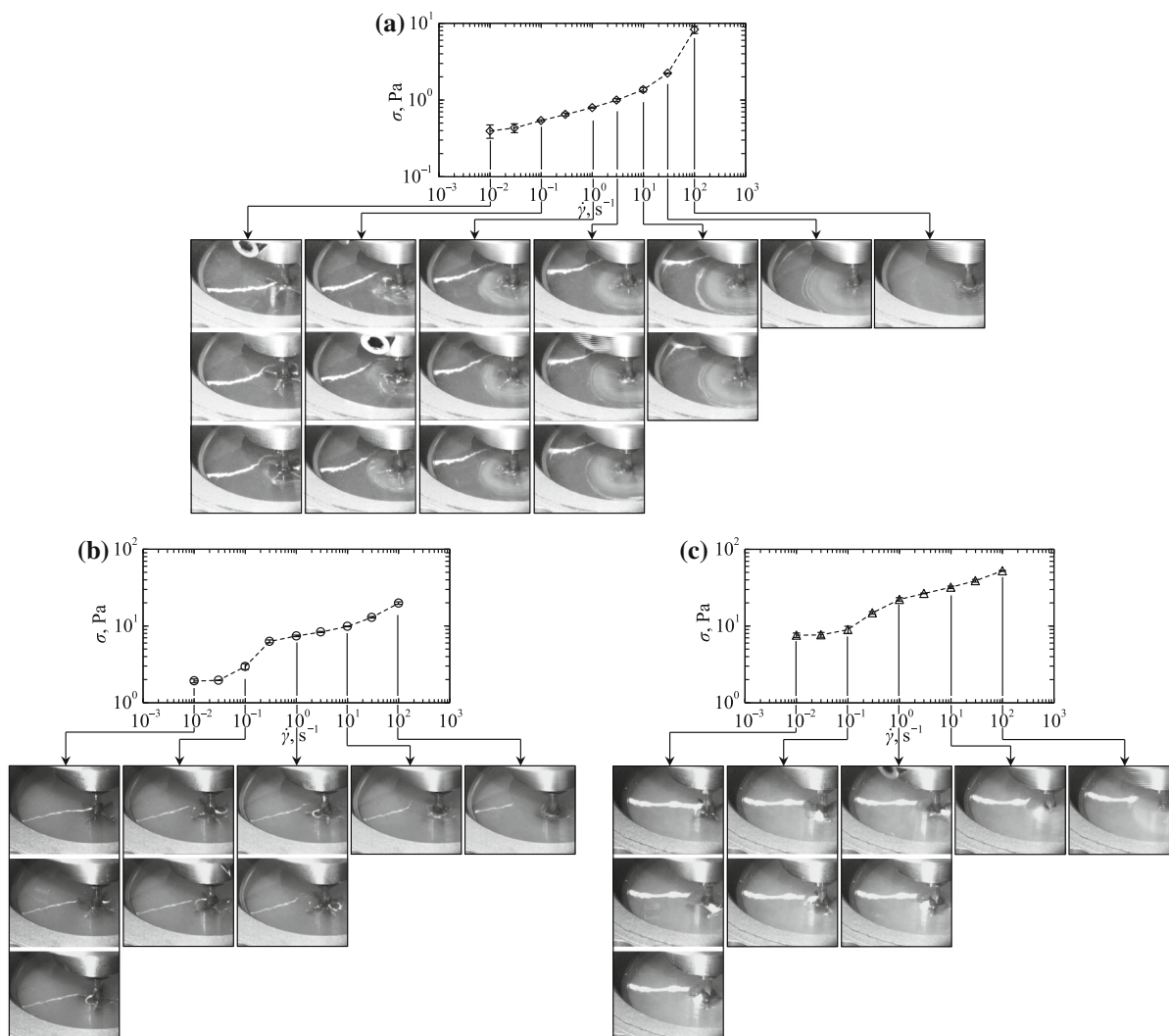


Fig. 4 Flow curves together with strain visualization of TEMPO-oxidized NFC suspensions at the concentrations of: **a** 0.5 wt%, **b** 1.0 wt% and **c** 1.5 wt% examined using vane-in-cup geometry

visual observations of the sample flow were not reported in the aforementioned work. Moreover, the cellulose sources and the production processes of TEMPO-oxidized NFC are different between two works, as well as the dimensions of the used geometries.

Roughening of the bob and cup surfaces was performed to compete with the wall-slip by attaching sandpaper. Figure 5 shows the flow curves of the NFC suspensions at different concentrations examined using serrated Couette geometry. As seen from Fig. 5a this approach was efficient to prevent the slip at the boundary of bob and the suspension at the concentration of 0.5 wt% due to the cohesive contact. However,

some volume of the sample remains undeformed within the experiment and it decreases with the increase of shear rate. At higher NFC concentrations (Fig. 5b, c) the flow instabilities become more apparent, similarly to the previous experiments.

The flow curves obtained using Couette and vane-in-cup geometries are compared in Fig. 6. The measured shear stress differs significantly at low shear rates and varies less at high ones. The highest stress response at low shear rates is observed when using serrated Couette geometry due to the strong cohesion between the NFC suspension and the geometry tools. The slightly lower stress is measured for the vane-in-cup

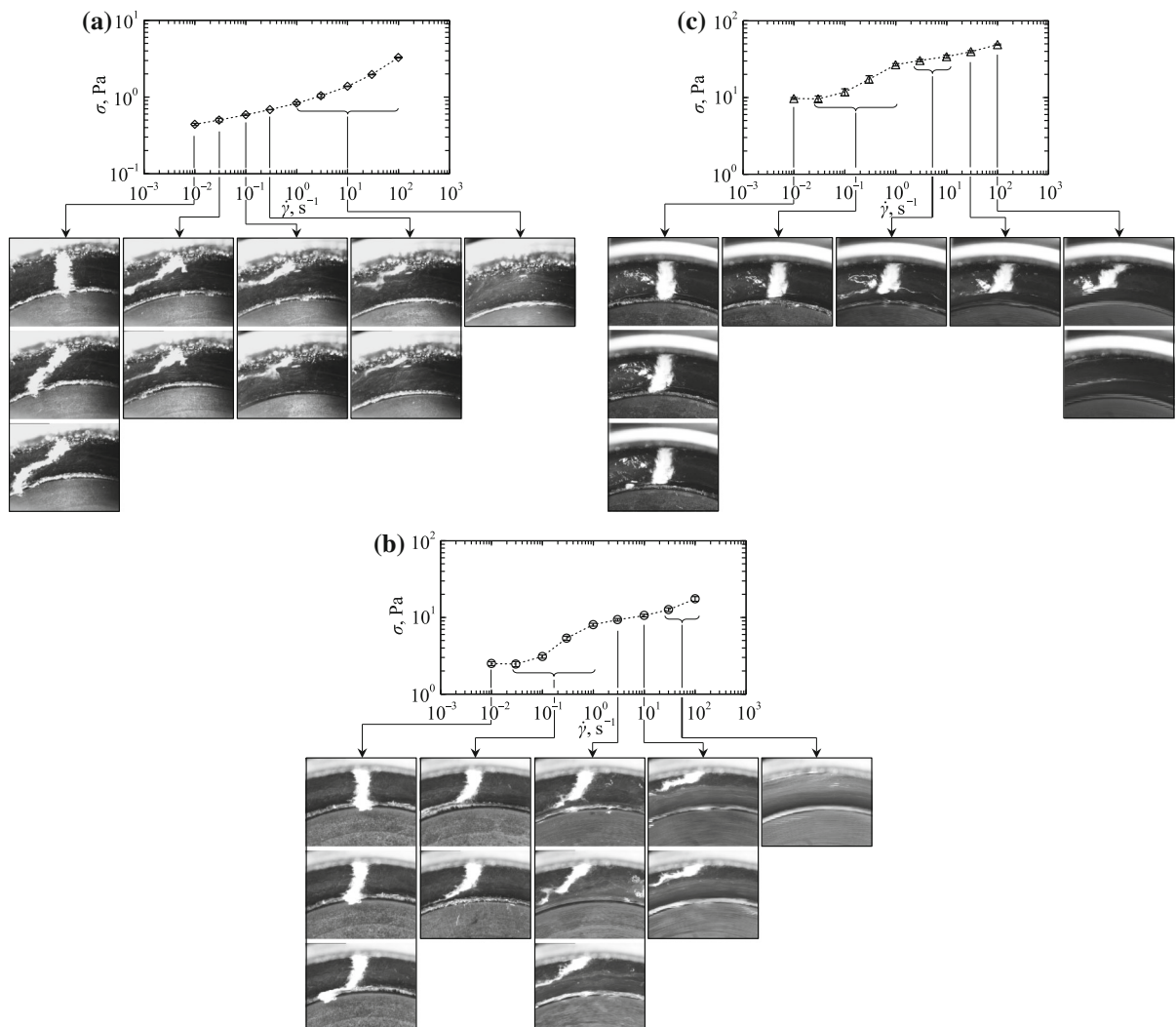


Fig. 5 Flow curves together with strain visualization of TEMPO-oxidized NFC suspensions at the concentrations of: **a** 0.5 wt%, **b** 1.0 wt% and **c** 1.5 wt% examined using serrated (roughened) Couette geometry

geometry, which is achieved by the contact at the surface between the suspension located in the gap of the geometry and that of trapped between the blades. In smooth Couette geometry the sample is in contact with a smooth bob surface, which makes its slipping easier and results in much lower level of the shear stress. A notable deviation from the other measurements is observed for the 0.5 wt% NFC suspension measured using vane geometry at the shear rate of 100 s^{-1} . Such dramatic increase of the shear stress can occur due to the secondary flows, which are more significant at high shear rates, caused by the specificity of the vane geometry. Such effect can also take place due to the

appearance of Taylor–Couette instabilities (Philippe et al. 2012) or turbulent flow (Beaumont et al. 2013).

Comparing the above results at low shear rates with those of obtained in the previous work when using smooth and serrated cone-plate geometries (Nechyporchuk et al. 2014), lower values of shear stress are obtained. This could be explained by the wider geometry gap in Couette and vane-in-cup geometries. At higher shear rates for Couette and vane-in-cup geometries, as well as cone-plate, the similar levels of shear stress are achieved. The samples start to flow; however, the measured stress level is still influenced by the shear banding in the bulk of the sample, which

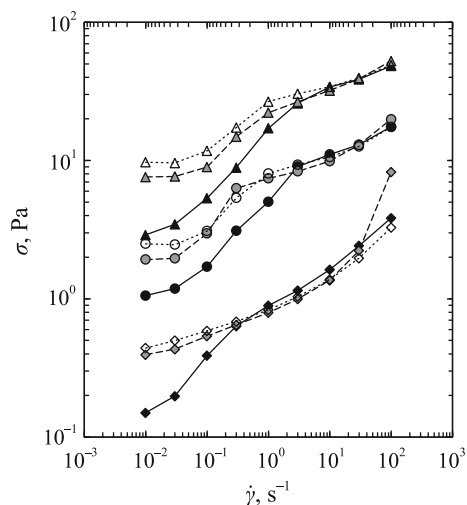


Fig. 6 Comparison of the flow curves of TEMPO-oxidized NFC suspensions obtained using smooth Couette (*filled symbols*), roughened Couette (*empty symbols*) and vane-in-cup (*half-filled symbols*) geometries at 0.5 wt% (*diamonds*); 1.0 wt% (*circles*) and 1.5 wt% (*triangles*)

becomes more significant with an increase of NFC concentration.

SAXS experiments

Figure 7a shows the radial average experimental scattering curves of the TEMPO-oxidized NFC suspensions at the concentrations of 0.1 and 0.5 wt% with the subsequent subtraction of water signal. The curves are obtained by radial integration of 2D SAXS patterns, as shown in Fig. 7b. The scattering intensities display a decline on the whole range of scattering vector. No influence of the NFC concentration on the shape of the curves is observed. Thus, there might be no influence on the interparticle interactions within the analyzed concentration range. The curves represent the scattering information about the elements of suspension at different magnifications: at low q the signal comes from the whole scattering objects and at high q from their interfaces.

The linear domains can be detected from the scattering curves, where the scattering intensity can fit the power law as specified in Eq. (2), which can give information about the structural organization of nanofibrils in suspension. $D = 3$ is a characteristic fractal dimension coming from rough surfaces, indicating the large objects, i.e., partially disintegrated fibers, with aggregated or entangled structure (van

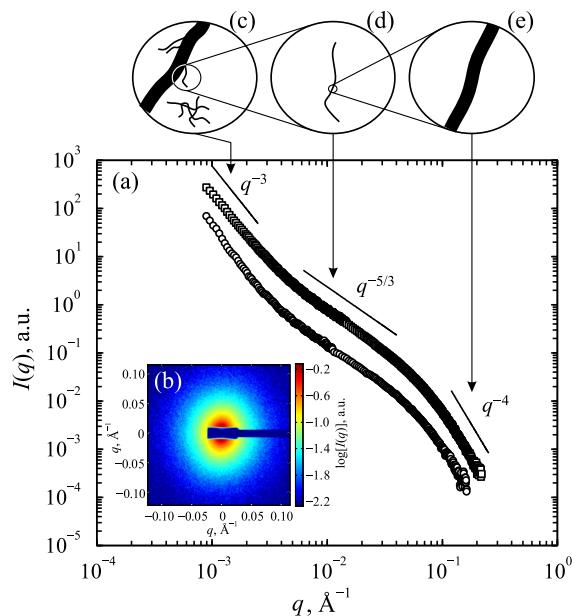


Fig. 7 SAXS characterization of TEMPO-oxidized NFC suspensions: **a** scattering intensity as a function of scattering vector for suspensions at the concentrations of: 0.5 wt% (*empty square*) and 0.1 wt% (*empty circle*); **b** typical two-dimensional SAXS pattern of the examined NFC suspensions; **c–e** schematic representation of the structures yielding the scattering signal

Duijneveldt et al. 2005). At higher scattering vector there is a slope where $D = 5/3$, which is a characteristic fractal dimension of swollen worm-like elements. It may represent the individual nanofibrils and determine their curvature. $D = 4$ (Porod law) indicates the non-fractal objects with smooth and well-defined interfaces, which is likely to appear from nanofibril interfaces. Each linear domain is preceded by a “shoulder”, representing the Guinier regime, which yields the size of the scattering objects. The Guinier regime located prior to the power-law regime with $D = 3$ is out of the measured range of scattering vector and is not represented in Fig. 7.

Thus, three structural levels can be determined from the experimental scattering data: (a) the first, coming from nanofibrils surfaces, as shown in Fig. 7e; (b) the second, which appears from individual nanofibrils, Fig. 7d, and (c) the third level, arising from partly disintegrated fibers or entanglements of the nanofibrils, Fig. 7c. Each structural level consists of Guinier and power-law regimes.

Two Guinier approximations can be verified at the first two structural levels as indicated in Fig. 7d, e. By drawing the Guinier plots, R_{gc} and R_g may be deduced

from the linear dependencies. Figure 8 shows no explicit linear regimes at Guinier plots, which makes it not possible to extract the information concerning the size of nanofibrils from Guinier approximations. This indicates that the system is polydisperse with continuous size distribution of particles diameter and length. The polydispersity of the examined NFC can be confirmed as well by the microscopy measurements, indicating the presence of the residual non-fibrillated fibers, as reported previously (Nechyporchuk et al. 2015). The aggregation of the nanofibrils is also expected due to hydrogen bonding. Moreover, the experiments were performed at pH of 7.0. Therefore, by increasing the pH, the concentration of carboxylate ions can be increased which will result in stronger electrostatic repulsion between the nanofibrils and possible decrease of aggregation.

The above Guinier approximation approach is applied when the interparticle interferences can be neglected. Otherwise, other methods should be used, e.g., generalized indirect Fourier transformation (GIFT), which allow the separation of inter- and intraparticle effects (Fritz et al. 2000). Such approach

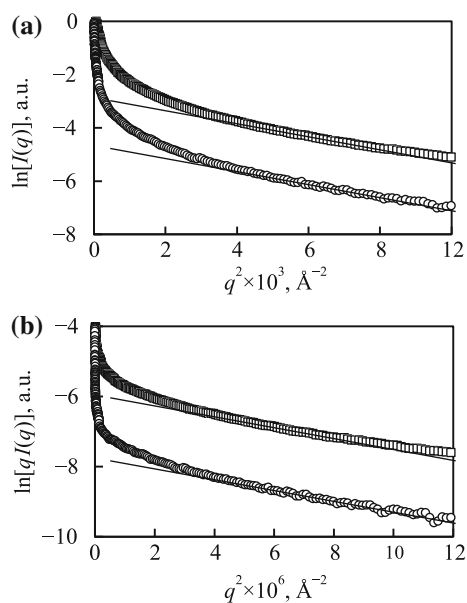


Fig. 8 Guinier approximations at **a** the second structural level representing the information arising from the individual nanofibrils in suspension and **b** the first structural level representing the scattering from the nanofibril cross-sections, at the concentrations of: 0.5 wt% (empty square) and 0.1 wt% (empty circle). Straight lines are presented to show the non-linearity of the Guinier plots

was already reported for suspensions of cellulose nanocrystals (Ehmann et al. 2013).

In this work the unified fit function approach was used to characterize NFC suspensions at different structural levels and to extract the average diameter of nanofibrils. Figure 9 shows the unified fit to the experimental data for the NFC suspension at the concentration of 0.5 wt% and the scattering functions from the local levels. The unified fit allows distinguishing the Guinier regions where considerable overlap with power-law regions takes place. At the first structural level the power-law region is quite short to perform the accurate analysis and to determine the exact power-law decay. Thus, the q range should be increased for more accurate analysis. Nevertheless, knowing that the analyzed material is fibrous, we can reasonably expect the power law decay with $P_1 = 4$. The third structural level is represented only by the power-law regime with $P_3 = 2.937$. To detect the Guinier regime at this level, the measurements at lower q , hence, higher sample-to-detector distance, should be performed.

The analyzed system consists of the nanofibrils that are flexible and curved, differing from the rod-like elements. Thus, the length of the nanofibrils cannot be extracted according to the Eq. (9). However, based on

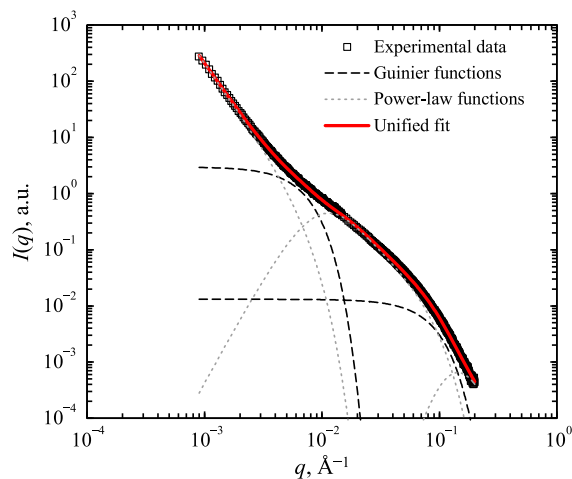


Fig. 9 The unified fit function (bold solid line) to the experimental scattering data (empty square) of the NFC suspension at the concentration of 0.5 wt% and the local scattering laws (dashed lines). The parameters of the local laws: $G_1 = 0.01312$; $G_2 = 2.977$; $R_{g,1} = 21.01 \text{ \AA}$; $R_{g,2} = 262.4 \text{ \AA}$; $B_1 = 7.68 \times 10^{-7}$; $B_2 = 1.46 \times 10^{-4}$; $B_3 = 3.27 \times 10^{-7}$; $P_1 = 4$; $P_2 = 1.912$; $P_3 = 2.937$

the scattering intensity coming from the nanofibrils cross-section, using Eq. (8), the nanofibrils diameter ($d = 2r$) can be calculated and was determined as 4.8 nm. This value represents the statistical average diameter of nanofibrils swollen in water and is in the range of 4 ± 2 nm, as demonstrated previously based on AFM height images (Nechyporchuk et al. 2015). It is worth noting that using AFM the nanofibrils are analyzed in the dry state, which can yield slightly lower diameter due to the nanofibrils shrinkage while drying. However, SAXS measurements allow determining the average diameter of nanofibrils swollen in water.

Conclusions

This work focuses on the characterization of TEMPO-oxidized NFC suspensions at different concentrations using rheometry and SAXS techniques. The flow instabilities are demonstrated for the first time in Couette and vane-in-cup geometries when using the visualization technique, where the strain field in the geometry gap was monitored through the deformation of the colored filament, made using titanium dioxide pigment. Such visualization enables to investigate the occurrence of the flow instabilities, like wall-slip and shear banding, in NFC suspensions.

The experiments performed using Couette geometry showed that the use of serrated geometry surfaces is necessary to compete with the wall-slip in NFC suspensions but is not sufficient to prevent it completely. These findings were compared to other data previously obtained with cone-plate geometries. The use of vane results in a fracture of the suspension at the edge of the blades, resembling the slip. It is obvious, that the slip is more crucial with an increase of the solid content in the suspension. The flow behavior depends strongly on the used geometry at low shear rates, where the wall-slip plays a significant role. However, at high shear rates the influence of the used geometry is neutralized, resulting in similar values of shear stress. Serrated Couette appeared as the most suitable geometry (among the tested) for the rheological measurements of NFC suspensions.

The polydispersity of the TEMPO-oxidized NFC was confirmed using SAXS analysis. It was shown that Guinier approximation is not effective to extract the size characteristics. However, the average diameter of

nanofibrils swollen in water was determined based on the scattering data using unified fit function approach.

Acknowledgments This work has been carried out within the framework of International Doctoral School in Functional Materials (IDS-FunMat, Erasmus Mundus) and was funded by French Ministry of Higher Education and Research. We would like to express our gratitude to European Synchrotron Radiation Facility (ESRF) and particularly to Theyencheri Narayanan for the support with SAXS measurements. We thank to Domsjö Fabriker AB for providing the cellulose pulp sample. Laboratoire Rhéologie et Procédés (LRP) and Laboratoire Génie des Procédés Papetiers (LGP2) are a part of the LabEx Tec 21 (Investissements d’Avenir—Grant Agreement No. ANR-11-LABX-0030) and PolyNat Carnot Institute (ANR-11-CARN-030-01). LGP2 is also a part of Energies du Futur Carnot Institute (ANR-11-CARN-007-01).

References

- Agoda-Tandjawa G, Durand S, Berot S, Blassel C, Gaillard C, Garnier C, Doublier JL (2010) Rheological characterization of microfibrillated cellulose suspensions after freezing. *Carbohydr Polym* 80:677–686. doi:10.1016/j.carbpol.2009.11.045
- Baravian C, Lalante A, Parker A (2002) Vane rheometry with a large, finite gap. *Appl Rheol* 12:81–87. doi:10.3933/ApplRheol-12-81
- Beaucage G (1995) Approximations leading to a unified exponential/power-law approach to small-angle scattering. *J Appl Cryst* 28:717–728. doi:10.1107/S0021889895005292
- Beaucage G (1996) Small-angle scattering from polymeric mass fractals of arbitrary mass-fractal dimension. *J Appl Cryst* 29:134–146. doi:10.1107/S0021889895011605
- Beaucage G (2012) Combined small-angle scattering for characterization of hierarchically structured polymer systems over nano-to-micron meter: part II theory. In: Matyjaszewski K, Möller M (eds) *Polymer science: a comprehensive reference*, vol 2. Elsevier BV, Amsterdam, pp 399–409
- Beaumont J, Louvet N, Divoux T, Fardin M-A, Bodiguel H, Lerouge S, Manneville S, Colin A (2013) Turbulent flows in highly elastic wormlike micelles. *Soft Matter* 9:735. doi:10.1039/c2sm26760h
- Benhamou K, Dufresne A, Magnin A, Mortha G, Kaddami H (2014) Control of size and viscoelastic properties of nanofibrillated cellulose from palm tree by varying the TEMPO-mediated oxidation time. *Carbohydr Polym* 99:74–83. doi:10.1016/j.carbpol.2013.08.032
- Besbes I, Magnin A, Boufi S (2011) Rheological behavior of nanofibrillated cellulose/acrylic polymer nanocomposites: effect of melt extrusion. *Polym Compos* 32:2070–2075. doi:10.1002/pc.21232
- Bonini C, Heux L, Cavaillé J-Y, Lindner P, Dewhurst C, Terech P (2002) Rodlike cellulose whiskers coated with surfactant: a small-angle neutron scattering characterization. *Langmuir* 18:3311–3314. doi:10.1021/la015511t
- Charani PR, Dehghani-Firouzabadi M, Afra E, Shakeri A (2013) Rheological characterization of high concentrated MFC

- gel from kenaf unbleached pulp. *Cellulose* 20:727–740. doi:[10.1007/s10570-013-9862-1](https://doi.org/10.1007/s10570-013-9862-1)
- Ehmann HMA, Spirk S, Doliška A et al (2013) Generalized indirect Fourier transformation as a valuable tool for the structural characterization of aqueous nanocrystalline cellulose suspensions by small angle X-ray scattering. *Langmuir* 29:3740–3748. doi:[10.1021/la303122b](https://doi.org/10.1021/la303122b)
- Elazzouzi-Hafraoui S, Nishiyama Y, Putaux J-L, Heux L, Dubreuil F, Rochas C (2008) The shape and size distribution of crystalline nanoparticles prepared by acid hydrolysis of native cellulose. *Biomacromolecules* 9:57–65. doi:[10.1021/bm700769p](https://doi.org/10.1021/bm700769p)
- Estellé P, Lanos C, Perrot A, Amziane S (2008) Processing the vane shear flow data from Couette analogy. *Appl Rheol* 18:34037–34481. doi:[10.3933/AppRheol-18-34037](https://doi.org/10.3933/AppRheol-18-34037)
- Fritz G, Bergmann A, Glatter O (2000) Evaluation of small-angle scattering data of charged particles using the generalized indirect Fourier transformation technique. *J Chem Phys* 113:9733–9740. doi:[10.1063/1.1321770](https://doi.org/10.1063/1.1321770)
- Glatter O, Kratky O (1982) Small-angle X-ray scattering, Chapters 2.IV; 8.III. Academic Press, London
- Grüneberger F, Künniger T, Zimmermann T, Arnold M (2014) Rheology of nanofibrillated cellulose/acrylate systems for coating applications. *Cellulose* 21:1313–1326. doi:[10.1007/s10570-014-0248-9](https://doi.org/10.1007/s10570-014-0248-9)
- Herrick FW, Casebier RL, Hamilton JK, Sandberg KR (1983) Microfibrillated cellulose: morphology, and accessibility. In: Sarko A (ed) Proceedings of the ninth cellulose conference, applied polymer symposia, vol 37. Wiley, New York, pp 797–813
- Ilavsky J, Jemian PR (2009) Irena: tool suite for modeling and analysis of small-angle scattering. *J Appl Cryst* 42:347–353. doi:[10.1107/S0021889809002222](https://doi.org/10.1107/S0021889809002222)
- Iotti M, Gregersen ØW, Moe S, Lenes M (2011) Rheological studies of microfibrillar cellulose water dispersions. *J Polym Environ* 19:137–145. doi:[10.1007/s10924-010-0248-2](https://doi.org/10.1007/s10924-010-0248-2)
- Ishii D, Saito T, Isogai A (2011) Viscoelastic evaluation of average length of cellulose nanofibers prepared by TEMPO-mediated oxidation. *Biomacromolecules* 12:548–550. doi:[10.1021/bm1013876](https://doi.org/10.1021/bm1013876)
- Lasseguette E, Roux D, Nishiyama Y (2008) Rheological properties of microfibrillar suspension of TEMPO-oxidized pulp. *Cellulose* 15:425–433. doi:[10.1007/s10570-007-9184-2](https://doi.org/10.1007/s10570-007-9184-2)
- Leppänen K, Pirkkalainen K, Penttilä P, Sievänen J, Kotelnikova N, Serimaa R (2010) Small-angle X-ray scattering study on the structure of microcrystalline and nanofibrillated cellulose. *J Phys Conf Ser* 247:012030. doi:[10.1088/1742-6596/247/1/012030](https://doi.org/10.1088/1742-6596/247/1/012030)
- Lowys M-P, Desbrières J, Rinaudo M (2001) Rheological characterization of cellulosic microfibril suspensions. Role of polymeric additives. *Food Hydrocolloids* 15:25–32. doi:[10.1016/S0268-005X\(00\)00046-1](https://doi.org/10.1016/S0268-005X(00)00046-1)
- Mohtaschemi M, Dimic-Misic K, Puisto A, Korhonen M, Maloney T, Paltakari J, Alava MJ (2014) Rheological characterization of fibrillated cellulose suspensions via bucket vane viscometer. *Cellulose* 21:1305–1312. doi:[10.1007/s10570-014-0235-1](https://doi.org/10.1007/s10570-014-0235-1)
- Naderi A, Lindström T, Sundström J (2014) Carboxymethylated nanofibrillated cellulose: rheological studies. *Cellulose* 21:1561–1571. doi:[10.1007/s10570-014-0192-8](https://doi.org/10.1007/s10570-014-0192-8)
- Nechporchuk O, Belgacem MN, Pignon F (2014) Rheological properties of micro-/nanofibrillated cellulose suspensions: wall-slip and shear banding phenomena. *Carbohydr Polym* 112:432–439. doi:[10.1016/j.carbpol.2014.05.092](https://doi.org/10.1016/j.carbpol.2014.05.092)
- Nechporchuk O, Pignon F, Belgacem MN (2015) Morphological properties of nanofibrillated cellulose produced using wet grinding as an ultimate fibrillation process. *J Mater Sci* 50:531–541. doi:[10.1007/s10853-014-8609-1](https://doi.org/10.1007/s10853-014-8609-1)
- Pääkkö M, Ankerfors M, Kosonen H, Nykänen A, Ahola S, Österberg M, Ruokolainen J, Laine J, Larsson PT, Ikkala O, Lindström T (2007) Enzymatic hydrolysis combined with mechanical shearing and high-pressure homogenization for nanoscale cellulose fibrils and strong gels. *Biomacromolecules* 8:1934–1941. doi:[10.1021/bm061215p](https://doi.org/10.1021/bm061215p)
- Penttilä PA, Várnai A, Fernández M, Kontro I, Liljeström V, Lindner P, Siika-aho M, Viikari L, Serimaa R (2013) Small-angle scattering study of structural changes in the microfibril network of nanocellulose during enzymatic hydrolysis. *Cellulose* 20:1031–1040. doi:[10.1007/s10570-013-9899-1](https://doi.org/10.1007/s10570-013-9899-1)
- Philippe AM, Baravian C, Jenny M, Meneau F, Michot LJ (2012) Taylor–Couette instability in anisotropic clay suspensions measured using small-angle X-ray scattering. *Phys Rev Lett* 108:254501. doi:[10.1103/PhysRevLett.108.254501](https://doi.org/10.1103/PhysRevLett.108.254501)
- Puisto A, Illa X, Mohtaschemi M, Alava M (2012) Modeling the rheology of nanocellulose suspensions. *Nord Pulp Pap Res J* 27:277–281
- Saarikoski E, Saarinen T, Salmela J, Seppälä J (2012) Flocculated flow of microfibrillated cellulose water suspensions: an imaging approach for characterisation of rheological behaviour. *Cellulose* 19:647–659. doi:[10.1007/s10570-012-9661-0](https://doi.org/10.1007/s10570-012-9661-0)
- Saarinen T, Lille M, Seppälä J (2009) Technical aspects on rheological characterization of microfibrillar cellulose water suspensions. *Annu Trans Nord Rheol Soc* 17:121–130
- Saito T, Nishiyama Y, Putaux J-L, Vignon M, Isogai A (2006) Homogeneous suspensions of individualized microfibrils from TEMPO-catalyzed oxidation of native cellulose. *Biomacromolecules* 7:1687–1691. doi:[10.1021/bm060154s](https://doi.org/10.1021/bm060154s)
- Saito T, Kimura S, Nishiyama Y, Isogai A (2007) Cellulose nanofibers prepared by TEMPO-mediated oxidation of native cellulose. *Biomacromolecules* 8:2485–2491. doi:[10.1021/bm0703970](https://doi.org/10.1021/bm0703970)
- Shogren RL, Peterson SC, Evans KO, Kenar JA (2011) Preparation and characterization of cellulose gels from corn cobs. *Carbohydr Polym* 86:1351–1357. doi:[10.1016/j.carbpol.2011.06.035](https://doi.org/10.1016/j.carbpol.2011.06.035)
- Terech P, Chazeau L, Cavaille JY (1999) A small-angle scattering study of cellulose whiskers in aqueous suspensions. *Macromolecules* 32:1872–1875. doi:[10.1021/ma9810621](https://doi.org/10.1021/ma9810621)
- Turbak AF, Snyder FW, Sandberg KR (1983) Microfibrillated cellulose, a new cellulose product: properties, uses, and commercial potential. In: Sarko A (ed) Proceedings of the ninth cellulose conference, applied polymer symposia, vol 37. Wiley, New York, pp 815–827
- van Duijneveldt JS, Klein S, Leach E, Pizzey C, Richardson RM (2005) Large scale structures in liquid crystal/clay colloids. *J Phys Condens Matter* 17:2255. doi:[10.1088/0953-8984/17/15/001](https://doi.org/10.1088/0953-8984/17/15/001)